PHOTONICS Research

Configurable microcavity-enhanced graphene photothermoelectric terahertz detectors

Yifan Yao,[1] Miao Cai,[1] Jingjing Fu,[1] Shicong Hou,[1] Yating Cai,[1] Fei He,[1] Xuguang Guo,[1,*] and Yiming Zhu[1,2]

[1]Shanghai Key Laboratory of Modern Optical Systems, Terahertz Technology Innovation Research Institute, and Engineering Research Center of Optical Instrument and System, Ministry of Education, University of Shanghai for Science and Technology, Shanghai 200093, China
[2]e-mail: ymzhu@usst.edu.cn
*Corresponding author: xgguo@usst.edu.cn

Received 27 June 2024; revised 27 July 2024; accepted 7 August 2024; posted 8 August 2024 (Doc. ID 533949); published 1 October 2024

Terahertz (THz) detectors with high sensitivity, fast response speed, room temperature operation, and self-powered feature are the key component for many THz applications. Microcavity resonators can effectively improve the sensitivity of THz detectors. However, it is difficult to precisely evaluate the microcavity resonator induced such improvement in experiment. Here, we realize a configurable microcavity–antenna-integrated graphene photothermoelectric (PTE) THz detector. Through the microcavity–antenna hybrid structure, THz radiations are localized and enhanced at one end of the graphene channel, and the temperature difference along the channel is greatly increased, resulting in the strong enhancement of PTE response. At the resonant frequency, the device has a high responsivity (976 V/W), low noise equivalent power (2.87 pW/Hz$^{1/2}$), and fast response speed (300 ns) at room temperature and in zero-bias operation mode. The microcavity-induced peak enhancement factor of 13.14 is accurately extracted. The microcavity–antenna introduced enhancement is further confirmed by using a two-temperature heat transfer model. The strategy of using a configurable microcavity is useful for further optimizing THz detectors by introducing the critical coupling mechanism.

https://doi.org/10.1364/PRJ.533949

1. INTRODUCTION

The terahertz (THz, 0.1–10 THz) detector is a crucial component in THz applications. The well-developed THz detectors include the Golay cell [1], quantum-well photodetector [2], bolometer [3], pyroelectric detector [4], plasma-wave detector [5], and so on. The performance of THz detectors is constantly improving with the discovery and application of new detection mechanisms and new materials [6–8]. However, until now the comprehensive performance of the existing THz detectors is far from meeting the needs of various THz applications. It is particularly important to develop THz detectors with room temperature operation, self-powered feature, high sensitivity, high dynamic range, and fast response.

The Dirac-cone band structure of graphene [9,10] determines its high carrier mobility [11,12] and wide spectral absorption [13,14], which are suitable for developing infrared and THz detectors. Soon after the discovery of graphene, the first batch of THz detectors based on graphene [7,15–18] was demonstrated. Compared with other types of detectors, photothermoelectric (PTE) detectors have the advantages of room temperature operation [15], zero bias, and broadband response. Due to the excellent thermoelectric properties and hot-carrier effect of graphene [19–21], it is a dominant candidate for the realization of high-performance THz PTE detectors. However, the low absorption efficiency of thin-layer graphene is a severe limit factor.

As a basic resonant mechanism, the Fabry–Perot (FP) resonance of a microcavity is widely used in visible and infrared photodetectors [22–27]. Microcavity-enhanced THz detectors began to be demonstrated [28,29]. The mechanical exfoliation process is usually utilized to fabricate graphene and other two-dimensional material photodetectors. However, due to the poor repeatability of mechanically exfoliated graphene, it is difficult to accurately evaluate the enhancement factor and other effects related to microcavity. In the THz band, the wavelength (λ) of the electromagnetic wave is in the 30–3000 μm range, so for the fundamental FP mode, the microcavity thickness ($\lambda/4n$ with n the refractive index of the substrate) is close to the device substrate thickness. Direct evaluation of the microcavity enhancement effects can be achieved by mounting a metallic mirror at the bottom of the substrate.

In this paper, based on the traditional asymmetric antenna coupling structure, we introduce a configurable microcavity–antenna hybrid structure, and use the FP resonance of the microcavity to further enhance the PTE response. Thus, the microcavity-related enhancement factor is directly obtained

experimentally. First, we use the finite-difference time-domain method (FDTD) electromagnetic simulation software (Lumerical Solutions) to optimize the structural parameters of the antenna and the microcavity, so that the open-circuit dipole resonant frequency of the antenna is consistent with the first FP resonant frequency of the microcavity. Then, the devices were fabricated by using the standard semiconductor planar process, graphene mechanical exfoliation, and the graphene fixed-point transfer. The experimental results are in good agreement with the theoretical design. This microcavity–antenna hybrid structure can achieve an excellent asymmetric heating effect near the designed resonant frequency to achieve high detection performance at room temperature and in zero-bias operation mode. The microcavity-induced peak enhancement factor of 13.14 is precisely derived. A two-temperature heat transfer model is implemented to relate the maximum temperature to the input THz power density, which further confirms the strong electric field enhancement induced by the microcavity–antenna structure. The configurable microcavity structure demonstrated in this paper provides a new and general solution for improving THz detection sensitivity and investigating microcavity-related critical coupling and strong coupling phenomena.

2. STRUCTURAL DESIGN AND SAMPLE PREPARATION

Figure 1 shows the schematic of the device structure and the research scheme of this work. Figure 1(a) is the structure and working principle of the graphene PTE detector. The detector is composed of three layers. The top layer is the asymmetric Au dipole antenna, the graphene channel, and the source and drain electrodes; the middle layer is the high-resistance silicon substrate; and the bottom layer is the demountable Au mirror attached on a silicon substrate. Thus, the microcavity–antenna structure is configurable, and the microcavity-induced enhancement effect can be directly evaluated by comparing the responsivities of the detector with and without the bottom Au mirror. When there is no Au mirror, the detector is a two-port device. Part of the incident THz wave will directly pass through the structure, and the maximum absorption is 50%. If the Au mirror is mounted, the incident THz wave is totally reflected back by the bottom Au mirror. In this case the detector becomes a one-port device, and the maximum absorption can reach up to 100% (critical coupling). By optimizing the length of the dipole antenna and the thickness of the high-resistance silicon, the dipole resonance of the structure can be consistent with the fundamental FP resonant frequency, forming a strong resonant coupling for the microcavity–antenna structure. When linearly polarized THz plane waves with the polarization direction along the y axis are normally incident along the z direction, if the frequency of the THz wave is consistent with the microcavity–antenna resonant frequency, strong local field enhancement can be obtained at the antenna feed slot. Because the resonant behaviors of the microcavity are very sensitive to the loss and the other device parameters, it is important to precisely evaluate the microcavity-induced resonant effects for achieving the strongest field enhancement. The proposed configurable microcavity–antenna structure provides a useful platform to reveal the effects of microcavity by comparing the detection parameters of the detector with and without the bottom Au mirror, respectively. Figure 1(b) shows the schematic diagram of the current-voltage (IV) curve of the PTE detector under THz irradiation, from which the open-cir-

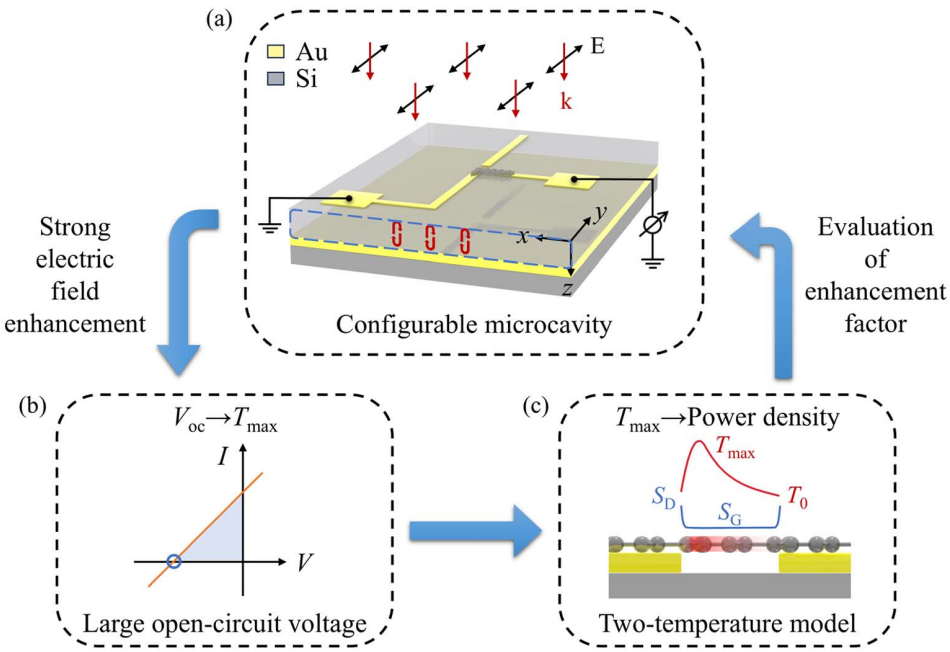

Fig. 1. (a) The schematic diagram of the FP resonance principle of the device. The microcavity enhancement effect can be directly obtained by measuring the detection performances of the device with and without the bottom Au mirror, respectively. (b) The schematic diagram of IV curve with THz irradiation. (c) The schematic diagram of the two-temperature heat transfer model, the hot electron temperature (red line) and Seebeck coefficient (blue line) distributions along the graphene channel.

cuit PTE voltage V_{OC} and then the maximum temperature of electron in the graphene channel can be derived. Figure 1(c) shows the two-temperature heat transfer model [30]. In the graphene channel, due to the weak electron–phonon interaction, the temperature of the electrons is much higher than that of the lattice when the device is irradiated by THz waves. The two-temperature heat transfer model can describe this feature and build a relation between electron temperature distribution and those relevant parameters (input power density, heat relaxation rate, thermal conductivity, and heat capacity). One end of the channel is in contact with one arm of the dipole antenna, and the other end is in contact with the metal electrode. Part of the graphene flake is located in the feed slot of the antenna. When a resonant THz wave normally irradiates the device, a strong local field enhancement is achieved in the feed slot of the dipole antenna, one end of the graphene flake is heated, and an asymmetric temperature difference is formed in the channel. The generated thermoelectric open-circuit voltage is

$$V_{OC} = \int \nabla T \cdot S(T, \varepsilon_F) \mathrm{d}x, \tag{1}$$

where T is temperature, S is the Seebeck coefficient, and ε_F is the Fermi energy. Figure 1(c) shows the diagrammatic sketch of the temperature and Seebeck coefficient distributions along the graphene channel. The change of Seebeck coefficient of graphene near the metal–graphene interface is due to the metal-induced doping. For simplicity, we assume the constant Seebeck coefficients S_G and S_D for the main channel and near the interfaces, respectively. According to Fig. 1(c), the thermoelectric response can be written as

$$V_{OC} = (S_G - S_D) \cdot (T_0 - T_{max}). \tag{2}$$

When the PTE open-circuit voltage V_{OC} is measured, the maximum electron temperature T_{max} is derived according to Eq. (2). Further, the input THz power density can be estimated through the two-temperature heat transfer model, which provides another way to determine the enhancement factor of the microcavity–antenna structure.

The designed resonant frequency is set to 90–100 GHz. We use FDTD electromagnetic simulation software to calculate the reflection spectra of different thick high-resistance silicon slabs with an Au mirror mounted at the back side. The complex permittivity of Au is given by the Drude model $\varepsilon_m = 1 - \omega_p^2/(\omega^2 + i\gamma_p\omega)$. The plasma frequency of Au $\omega_p = 1.12 \times 10^{16}$ rad/s, scattering coefficient $\gamma_p = 8.67 \times 10^{13}$ rad/s, ω is the angular frequency of incident light, and i is the imaginary unit.

As shown in Fig. 2(a), the first-order reflection peak of the high-resistance silicon slab with an Au mirror is inversely proportional to the thickness of the silicon slab, and the width of the reflection peak decreases with the increase of the substrate thickness. The high-order reflection peaks of the structure show similar rules with the change of silicon thickness. The above reflection behavior has typical FP resonant characteristics. The FP resonant wavelength λ can be described by $2nl = k\lambda - \lambda/2$, where l is the thickness of the silicon slab, and k is the order of the reflection peak, which is consistent with the numerical simulation results. According to the simulation results, we selected a high-resistance silicon wafer with a

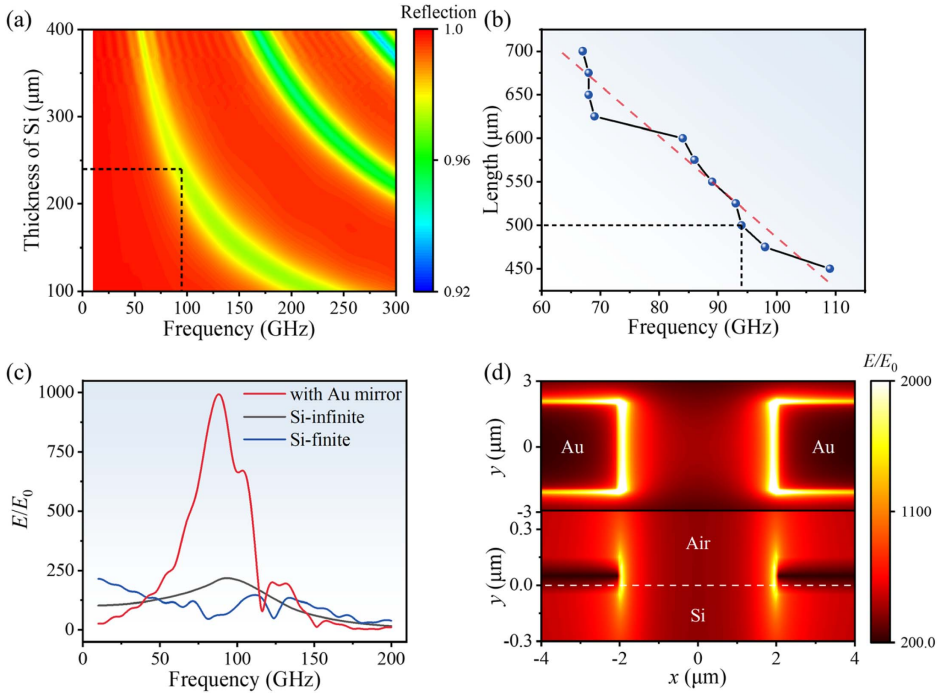

Fig. 2. (a) The reflection spectra of a silicon slab with different thicknesses and an Au mirror mounted at the bottom of the slab. (b) The schematic diagram of the resonant frequency of the dipole antenna with different arm lengths. (c) The surface-averaged electric field enhancements in the feed slot region as functions of frequency for the cases of infinite silicon substrate, 243-μm thick silicon slab, and 243-μm thick silicon slab with an Au mirror mounted at the bottom, respectively. The single arm length of the antenna is 500 μm. (d) The surface electric field distribution (top) and vertical electric field distribution (bottom) in the feed slot region at the resonant frequency of 95 GHz of the microcavity–antenna structure.

nominal thickness of 240 μm, whose resistivity is greater than 10,000 Ω/cm, and its THz absorption can be ignored. We use a THz time-domain spectroscopy (THz-TDS) system to measure the transmission spectrum of the silicon wafer, as shown in Fig. 7 (Appendix A). The actual thickness of the silicon wafer is calculated to be about 243 μm [Eqs. (A1) and (A2) in Appendix A].

In order to observe the dipole-FP resonant behavior more clearly, we choose the narrow-band dipole antenna as the receiving antenna of the detector. In order to match the operating frequency of the designed detector, we still use the FDTD software to simulate the resonant frequency of the dipole antenna with different lengths. The resonant frequency of the dipole antenna is roughly determined using the formula $h \approx \lambda/2 \approx 700$ μm [31], where h is the length of one single arm. The numerical results of the resonant frequency as a function of the single arm length are shown in Fig. 2(b). With the decrease of the single arm length, the resonance frequency of the antenna shifts to high frequency, showing an approximate linear relationship. As shown in Fig. 2(b), the single arm length of 500 μm is selected to match the FP resonance of the silicon microcavity, and strong field localization and enhancement are expected.

To verify the resonant behavior of the microcavity–antenna structure, the electric field enhancement factors (defined as E/E_0 with E the averaged electric field intensity in the feed slot region and E_0 the electric field intensity at the surface of infinite silicon substrate without the antenna structure) in the feed slot with frequency of the dipole antenna on three different substrates, infinite thickness silicon, finite thickness silicon slab (243 μm thick), and finite thickness silicon slab (243 μm thick) with an Au mirror at the bottom side are numerically calculated using the FDTD software. As shown in Fig. 2(c), due to the antenna-introduced lateral focusing of the electromagnetic field, there are strong electric field enhancements in the slot regions for all the three structures. As expected, the microcavity–antenna structure leads to the largest electric field enhancement factor of 993 (red line), and for the other structures the enhancement factors are 218 (silicon slab, gray line) and 147 (infinite silicon substrate, blue line), respectively. The numerical results show that when the dipole antenna resonance is coupled with the FP resonance, the electric field enhancement factor can be increased by about 4 times. Figure 2(d) is the numerical electric field intensity in the feed slot for the microcavity–antenna structure. It can be seen that the electric field intensity in the feed slot is greatly enhanced, especially near the metallic edges.

We used the traditional two-dimensional material processing technology to fabricate the device, and the detailed process is shown in Fig. 8 (Appendix B). As shown in Fig. 3(a), the dipole antenna is directly deposited on the high-resistance silicon substrate. Detailed information of the feed slot and the graphene channel is shown in Fig. 3(b). Two van der Waals electrical contacts are expected to form between the graphene channel and the two electrodes. Near the resonant frequency, the normally incident y-polarized THz waves ensure a good asymmetric heating to produce a large temperature difference between the two electrodes. The atomic force microscope (AFM) image of the feed slot region is presented in Fig. 3(c), from which the graphene flake thickness of about 20 nm is obtained. Such a thick multilayer graphene channel will ensure a large THz absorption. In order to characterize the metal–graphene contacts, we used a semiconductor parameter analyzer (Keithley 4200A-SCS) to measure the dark IV curve. Figure 3(d)

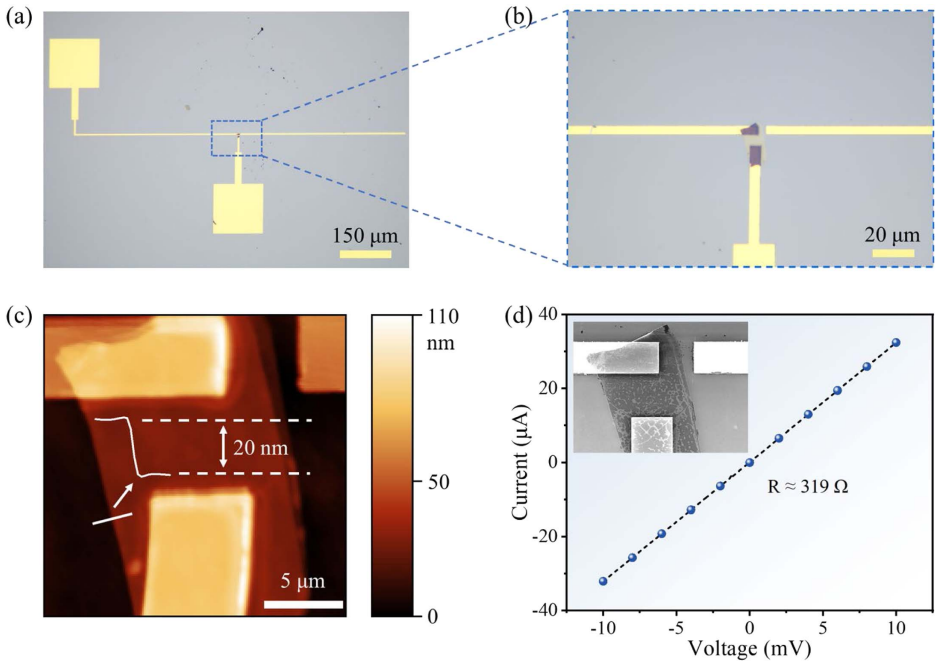

Fig. 3. Optical microscope images of the asymmetric antenna coupled THz PTE detectors with a magnification of 100 (a) and the detailed structure near the feed slot region with a magnification of 500 (b). (c) The AFM image of the graphene channel. Inset is the AFM line profile. (d) IV characteristic curve of the device. Inset is the scanning electron microscope (SEM) image of the graphene channel with a magnification of 3500.

is the dark *IV* curve of the device, which shows that there are good Ohmic contacts between the graphene channel and the metal electrodes, and the resistance of the device is about 319 Ω.

3. RESULTS AND DISCUSSION

The electrical and optical properties of the microcavity–antenna integrated graphene detector are measured at room temperature (300 K). The THz source (VDI, WR10) is a frequency multiplier driven by a microwave source (Rohde & Schwarz, SMB100A), which can emit 75–110 GHz linearly polarized THz waves up to mW level. The details of the measurement system are shown in Fig. 9 (Appendix C). As shown in Fig. 4(a), the maximum short-circuit THz response current is up to 20 μA, showing an excellent THz detection performance. The response time of the detector is characterized by the rise time and fall time of a photocurrent pulse caused by a square-wave-modulated THz wave. The rise time is defined as the time when the photocurrent amplitude increases from 10% to 90%, and the fall time is the time when the photocurrent amplitude decreases from 90% to 10%. As shown in Fig. 4(b), the rise and fall times are 0.3 μs and 1.7 μs, respectively. The hot electron effect in graphene is responsible for the fast response.

Next, we measured the *IV* curves of the device under THz irradiation (red) and dark (blue) conditions. As shown in Fig. 4(c), the two *IV* curves are linear and parallel to each other, indicating that the photon response of the device is independent of the bias voltage, which is a typical feature of PTE response [32,33]. The open-circuit photon voltage [zero photocurrent point in Fig. 4(c)] is −6.1 mV. The Seebeck coefficient of graphene we used is 109 μV/K [34]. According to Eq. (1), it can be calculated that the asymmetric heating structure causes the temperature difference along the graphene channel to be about 56 K. Such a high temperature difference induced by the 1.0 mW/cm^2 incident radiation indicates that at the resonant frequency, the electromagnetic field energy is effectively localized into the feed slot by the microcavity–antenna coupling structure. The polarization-dependent response of the device was measured, and the experimental data are shown in Fig. 4(d). The polarization angles 0 and 90 deg correspond to the incident electric field parallel and perpendicular to the dipole antenna, respectively. The photocurrent is strongly dependent on the polarization of the incident wave. The good agreement between the measured photocurrent data (black dots) and the theoretical polarization-dependent gain of a dipole antenna (red line) indicates that the excellent photoresponse of the device is mainly contributed by the microcavity–antenna coupling structure. The photoresponse at different modulation frequencies and output power can be seen in Fig. 9 (Appendix C).

As shown in Fig. 5(a), for a fixed frequency (99 GHz) of THz radiation, the photocurrent exhibits an attenuated oscillation with respect to the distance *d* between the emission port and the detector, which has not been reported. Such an oscillation behavior is attributed to the multireflectance of the coherent THz wave between the emission port surface and the Au mirror at the bottom of the device substrate [insertion in Fig. 5(a)]. The attenuation of oscillation amplitude originates from the non-zero divergence angle and air loss of the THz wave. A double-cavity model is built to describe the photocurrent oscillation. Distance-dependent reflectivity is introduced

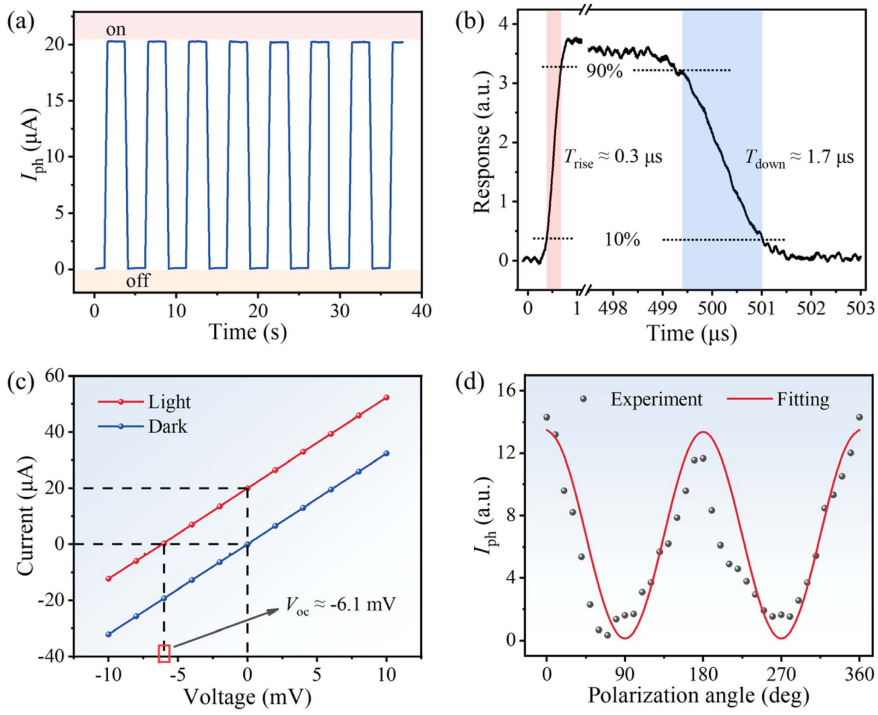

Fig. 4. Peak response of the microcavity–antenna integrated graphene detector at 99 GHz. (a) Pulse response current of the graphene PTE detector. (b) The rise and fall response times of the device. (c) The *IV* curves with and without THz irradiation. (d) Polarization-dependent response current of the device.

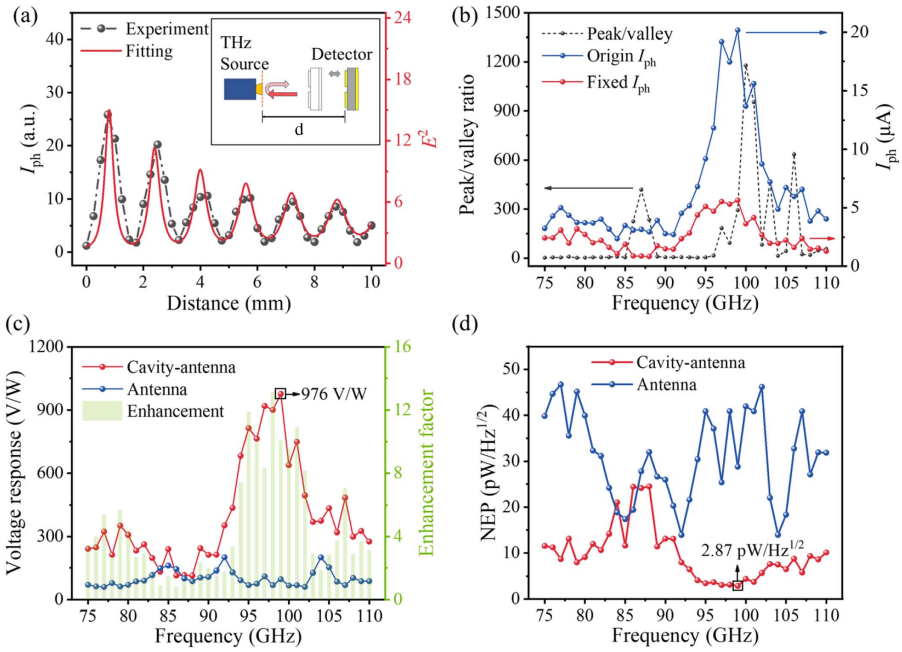

Fig. 5. (a) The photocurrent with respect to the distance d at frequency 99 GHz. Insert is the schematic diagram of the effective FP cavity composed of the emission port of the coherent THz source and the Au mirror at the bottom of device substrate. (b) The origin (blue) and fixed (red) photocurrent spectra. The voltage responsivity spectra of the device with (red) and without (blue) Au mirror mounted at the bottom of the substrate (c) and the corresponding noise equivalent power (NEP) (d).

as a fitting parameter to represent the effect of non-zero divergence angle and air loss. The details of the model are presented in Appendix D. The double-cavity model gives an excellent fitting to the experiment data [the red solid line in Fig. 5(a)]. In our experiment, the maximum photocurrent (the first oscillation peak) is recorded. With the assistance of the fitting curve, the ~3.74-fold pseudo enhancement of the photocurrent due to reflection from the emission port of the THz can be extracted. When the Au mirror is not mounted on the device, the double-cavity effect is greatly weakened, and the details are presented in Appendix D.

Once the origin of the photocurrent oscillation is addressed, another more convenient method can be adopted to acquire the real amplitudes of the photocurrent. The peak-to-valley ratio Γ of the photocurrent oscillation can be expressed as

$$\Gamma = \frac{(E_0 + E_1)^2}{(E_0 - E_1)^2}, \tag{3}$$

where E_0 is the electric field amplitude on the photoactive surface of detector without considering the reflection from the emission port, and E_1 is the reflection electric field amplitude. When Γ is measured, the real photocurrent can be evaluated using the expression

$$I_{ph} = I_{phm} \times \left(\frac{E_0}{E_0 + E_1}\right)^2 = I_{phm} \times \frac{(1 + \sqrt{\Gamma})^2}{4\Gamma}, \tag{4}$$

where I_{phm} is the measured photocurrent. Figure 5(b) shows the measured photocurrent, the value of Γ, and the evaluated real photocurrent with respect to frequency in the range of 75–110 GHz.

To evaluate the responsivity, the effective area of the device must be first determined. For the receiving antenna, there are several methods to calculate the effective receiving area [35]. One of the methods is to directly use the physical area of the antenna, which will give the maximum responsivity. Another method is to use the equivalent area of the antenna. The effective area A_{em} of a dipole antenna adopted in this work is given by the following expression [36]:

$$A_{em} = \frac{3}{8\pi}\lambda_{eff}^2, \tag{5}$$

where $\lambda_{eff} = 2\lambda_0/(n+1)$ is the effective wavelength, λ_0 is the wavelength in vacuum, and $n = 3.42$. The power density of the THz source is measured to be about $P = 1.0$ mW/cm^2 in the frequency range of 75–110 GHz. The voltage responsivity R_v is calculated by the following formula:

$$R_v = \frac{I_{ph}R}{PA_{em}}, \tag{6}$$

where R is the device resistance. The voltage responsivity spectrum (red solid line) of the microcavity–antenna coupled detector is shown in Fig. 5(c). Because the PTE response is expected to be independent of frequency in a small frequency range (75–110 GHz), the resonant responsivity spectrum is due to the microcavity–antenna coupler. In addition, the responsivity curve is in good agreement with the electric field enhancement curve (red solid line) shown in Fig. 2(c), which further identifies this point. The peak responsivity of 976 V/W indicates the high coupling efficiency of the microcavity–antenna structure.

In order to precisely evaluate the enhancement effect of the microcavity, the bottom Au mirror is removed, and the responsivity spectrum is measured at once, which minimizes the influences of the other device parameters and experimental conditions. A similar but weak double-cavity effect is observed. In this case, the cavity is formed between the emission port of the THz source and the bottom surface of the silicon substrate. However, due to the small reflectivity in the silicon–air interface, a nearly constant peak-to-valley ratio of 2 is derived. Using Eqs. (3)–(6), the responsivity spectrum (blue solid line) of the detector without the Au bottom mirror is achieved and shown in Fig. 5(c). Thus, the microcavity-induced enhancement factor with respect to frequency is derived, and the result (green pillar) is presented in Fig. 5(c). It can be seen that the microcavity introduces a remarkable enhancement of coupling efficiency.

Since the detector is operated in zero-bias mode, only thermal (Johnson–Nyquist) noise is considered. The Johnson–Nyquist voltage noise is $\sqrt{4k_B TR}$, where k_B is the Boltzmann constant and T is the operating temperature. The other extrinsic noises such as the residual flicker noise and the interference noises are not considered. In practical applications, the real detector sensitivity is dependent on the working condition and will be deteriorated to some extent in comparison with the intrinsic sensitivity. We utilized an electrical spectrum analyzer (Keysight, N9040B) to measure the voltage noise density spectrum of the device (Appendix C). At the modulation frequency of 1 kHz, the measured voltage noise is 2.8 $\mathrm{nV/Hz^{1/2}}$, which is utilized to calculate the NEP parameter. The NEP can be calculated as

$$\mathrm{NEP} = \frac{v_n}{R_V}, \tag{7}$$

where v_n is the voltage density and R_V is the voltage response. The NEP spectra of the device with (red solid line) and without (blue solid line) the bottom Au mirror are depicted in Fig. 5(d). For the microcavity–antenna coupled detector, the NEP is less than 10 $\mathrm{pW/Hz^{1/2}}$ in the frequency range of 92–110 GHz, and the minimum reaches 2.87 $\mathrm{pW/Hz^{1/2}}$ at 99 GHz, showing that the device has a very high room-temperature and zero-bias detection sensitivity. The superior detection performance is mainly attributed to the high coupling efficiency of the microcavity–antenna hybrid structure.

Finally, we further study the temperature distribution at the graphene channel, and we establish a one-dimensional two-temperature heat transfer model, as shown in Fig. 6(a). The width of the electrodes on both sides and the intermediate graphene channel is set to 4 μm. We assume that the THz electric field is focused in the range of 1 μm on the left side of the graphene channel. In the steady state, the electron and lattice temperatures satisfy the following equations [37]:

$$\nabla^2 T_e = \frac{C_e}{\kappa_e \tau_{ep}}[T_e(x) - T_p(x)] + \frac{C_e}{\kappa_e \tau}[T_e(x) - T_0] - \frac{Q(x)}{\kappa_e}, \tag{8}$$

$$\nabla^2 T_p = \frac{\rho_p C_p}{\kappa_p \tau}[T_p(x) - T_0] - \frac{C_e}{\kappa_p \tau_{ep}}[T_e(x) - T_p(x)], \tag{9}$$

$$\nabla^2 T = \frac{\rho C}{\kappa \tau}[T(x) - T_0], \tag{10}$$

where T_0 is the fixed environment temperature. T, κ, τ, and C are temperature, thermal conductivity, heat relaxation time to environment, and heat capacity for Au electrodes, respectively. T_e (T_p), κ_e (κ_p), and C_e (C_p) are temperature, thermal conductivity, and heat capacity for electron (lattice) subsystems of graphene. τ_{ep} is the heat relaxation time from electron subsystem to crystal subsystem. Q is the thermal source. ρ and ρ_p are the mass densities of Au and graphene.

The heat capacity of multilayer graphene can be expressed as [38,39]

$$C_e = m\frac{2\pi E_F}{3(v_F)^2}k_B^2 T_e, \qquad E_F \gg k_B T_e, \tag{11}$$

where m is the graphene layer number. The electron thermal conductivity is [39]

$$\kappa_e = \frac{C_e \mu_c E_F}{2e}, \tag{12}$$

where μ_c is the electron mobility in graphene. A direct iteration scheme is used to solve the coupled Eqs. (8)–(10).

When the THz field energy is focused on the left end of the graphene channel, the electrons form a large asymmetric temperature distribution, which leads to a strong PTE response. Excluding the enhancement of the standing wave to the response, the temperature difference along the graphene channel is about 15 K. Figure 6(b) shows the numerical electron and lattice temperature distributions. ΔT_e and ΔT_c are the temperature difference of electron and lattice. The parameter values taken in the calculation are listed in Table 2 (Appendix E). Due to the large heat capacity of the graphene lattice and the Au electrode, the temperature changes of the Au and graphene lattice are very small. To maintain the maximum temperature difference of about 15 K, the power density of THz radiation should be up to about 3×10^6 $\mathrm{W/m^2}$ in the feed slot region of the antenna. The power density in the feed slot can be evaluated as $P_0 \times \gamma^2 \approx 10^7$ $\mathrm{W/m^2}$, where $P_0 = 1$ $\mathrm{mW/cm^2}$ is the emission power density of the THz source, and $\gamma \approx 1000$ [Fig. 2(c)] is the peak electric field enhancement factor of the microcavity–antenna structure, which is qualitatively consistent with the input power density in the calculation of electron temperature distribution by solving Eqs. (8)–(10).

The peak temperature at the graphene channel is related to many parameters. As shown in Fig. 6(c), the peak electron temperature of graphene is linearly related to the incident power; other parameters are the same as in Fig. 6(b). Keeping the incident power 3×10^6 $\mathrm{W/m^2}$ constant, we change the relaxation time and thermal conductivity. As shown in Fig. 6(d), the abscissa is the hot carrier relaxation time τ to the environment, and the ordinate is the thermal conductivity κ_e of the graphene electron. The peak temperature of graphene increases with the increase of τ and decreases with the increase of κ_e.

As shown in Table 1, we compared the room temperature THz detectors based on graphene in recent years. It can be seen that the responsivity and NEP of the devices we developed are better than that of other detectors, the response time is also in the middle and upper level, and the comprehensive performance is higher.

A perfect absorber is very important for improving the detection sensitivity of a photodetector. As a one-port device, when the critical coupling condition is fulfilled, perfect

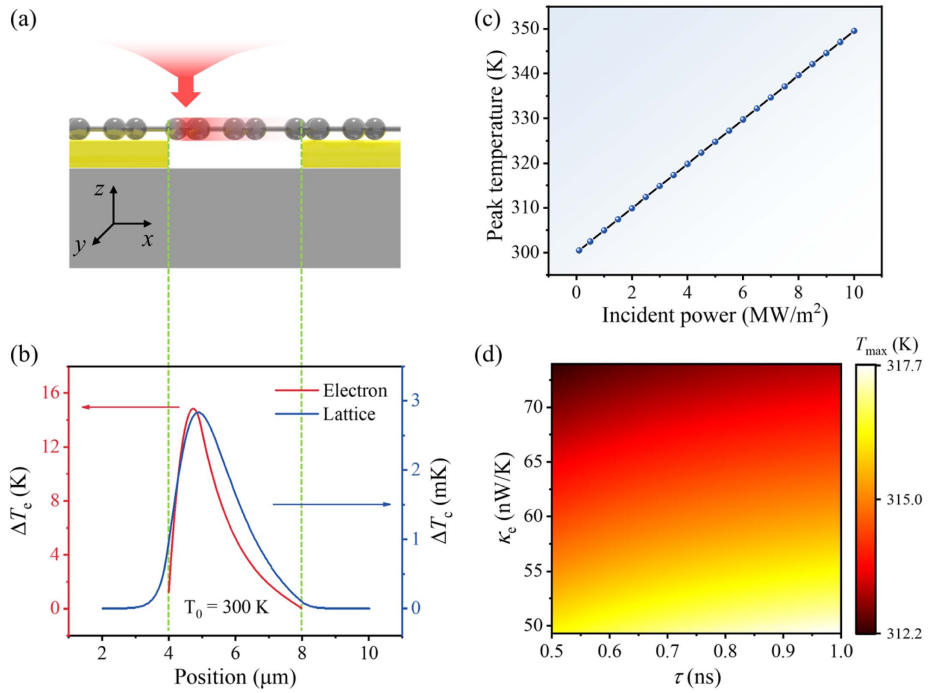

Fig. 6. (a) Structure diagram of the one-dimensional two-temperature heat transfer model. (b) Temperature distribution of the graphene electron and lattice between the source and drain electrodes. (c) The temperature difference between the graphene and electrode changes linearly with the incident power. (d) The variation of the maximum temperature difference between the graphene and electrode with heat relaxation time and electron heat capacity.

Table 1. Performance Comparison of Different Graphene-Based PTE THz Detectors

Operating Frequency (THz)	Voltage Responsivity (V/W)	NEP (pW/Hz$^{1/2}$)	Response Time (ns)	References
0.08–0.12	28	350	9×10^3	[40]
0.3	49	160	3.3	[41]
2.8	/	1×10^3	5	[42]
2.52	0.7×10^{-3}	1.43×10^6	45×10^6	[43]
2.52	37.1×10^{-3}	58×10^3	6.6×10^9	[44]
0.13	20	600×10^3	/	[45]
0.075–0.11	976	2.87	300	This work

absorption can occur for a microcavity structure. For example, in Ref. [46], Dai *et al.* demonstrated the perfect absorption in an infrared detector. In the THz band, perfect-absorber-based detectors have been reported [47]. At present, for the PTE THz detector, because the loss of graphene cannot be tuned, the critical coupling condition is not guaranteed.

4. CONCLUSION

In summary, a configurable microcavity–antenna coupled graphene THz detector is proposed and demonstrated. By optimizing the structural parameters of the dipole antenna and the microcavity, the fundamental dipole and FP modes of the hybrid structure are at the same frequency, which leads to the strong localization and enhancement of electric field in the feed slot region and the efficient asymmetric heating of the graphene channel. Therefore, the microcavity–antenna coupled detector exhibits an excellent PTE response in the frequency range of 75–110 GHz at room temperature and in zero-bias operation mode. Because the Au mirror is removable, the microcavity-introduced enhancement factor can be precisely evaluated, which provides a convenient and efficient way to investigate the microcavity-related effects such as the critical coupling and the strong coupling between the microcavity FP modes and other resonant modes. We believe that the detector performance can be further improved if the critical coupling condition is satisfied for the microcavity–antenna hybrid structure.

APPENDIX A: THICKNESS MEASUREMENT OF SILICON WAFERS

In order to obtain the thickness of the silicon wafer, we use a home-made THz-TDS system to measure the transmission spectrum of the silicon wafer [Fig. 7(a)]. We placed the silicon wafer at the focus of the THz-TDS optical path and measured

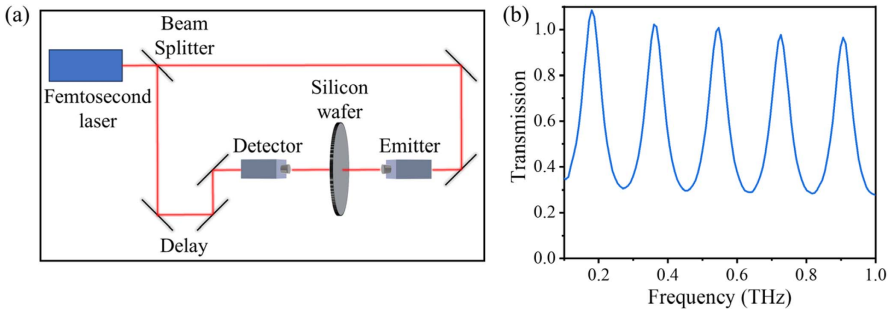

Fig. 7. (a) Schematic diagram of the measurement system. (b) THz transmission spectrum of silicon wafers.

the transmission spectrum of the silicon wafer for the THz wave with the air signal as the reference. As shown in Fig. 7(b), the transmission spectrum of the silicon wafer shows perfect Fabry–Perot oscillations. The refractive index of the silicon wafer can be calculated from Eq. (A1):

$$n = \sqrt{\frac{2\sqrt{1-a}}{a} + \frac{2}{a} - 1}, \tag{A1}$$

where a is the transmission coefficient and n is the refractive index.

The thickness of the silicon wafer can be calculated by Eq. (A2):

$$d = \frac{2m-1}{4nf}, \tag{A2}$$

where m is the order of the transmission peak and f is the frequency of the transmission peak.

APPENDIX B: DEVICE FABRICATION PROCESS FLOW

The fabrication process of the device is mainly divided into four steps, as shown in Fig. 8. The first step is electron beam lithography (EBL), and the antenna pattern is defined on the surface of the silicon wafer; the second part is thermal evaporation, which attaches Au to the surface of silicon wafer; the third step is lift off, stripping the excess Au from the surface of the silicon wafer; and the fourth step is the transfer of the multilayer graphene flake, where the graphene is transferred to the channel of the antenna through the polydimethylsiloxane (PDMS) film.

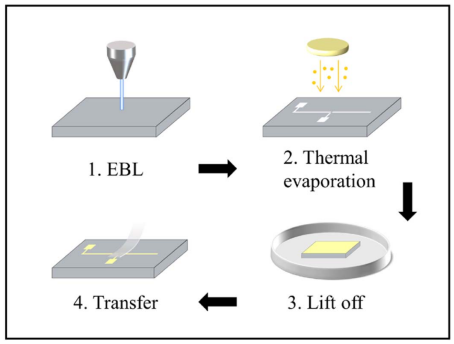

Fig. 8. Schematic diagram of device fabrication.

APPENDIX C: DEVICE MEASUREMENT

The device measurement system is shown in Fig. 9. We utilized an RF and microwave signal generator as the primary source. The output microwave is set to square-wave-modulated waveform (the modulation depth, 100%; the modulation frequency, 1 kHz). The RF and microwave signal generator was used to drive the frequency multiplier. The terahertz beam is directly emitted to free space through a horn antenna without collimation, and the detector is placed in front of the horn antenna. The short-circuit photocurrent signal of the detector is amplified by the pre-current amplifier. The output voltage signal is sent to the lock-in amplifier and the oscilloscope at the same time. The amplitude of the signal is read directly by the lock-in amplifier, and the response signal waveform is observed by the oscilloscope.

Due to the ultra-high hot carrier mobility in graphene, the graphene detector is expected to have a fast response speed. The photocurrent amplitude of the detector maintains a constant value when the modulation frequency of the THz wave is in the range of 1–20 kHz [Fig. 10(a)], which indicates that the corresponding cutoff frequency is much higher than 20 kHz. Due to the limitation of the modulation speed of our emitter, the high-frequency behavior of our device has not been characterized. In addition, we measured the power-dependent optical response at a fixed frequency of 14.8 GHz and observed a good linear power dependence [Fig. 10(b)]. It shows that our detector has a large dynamic range.

Figure 11 shows the voltage noise density spectrum of the device. At the low-frequency region, the $1/f$ noise takes the dominant position. With the increase of frequency, the $1/f$ noise decreases. The measured voltage noise is 2.8 $nV/Hz^{1/2}$

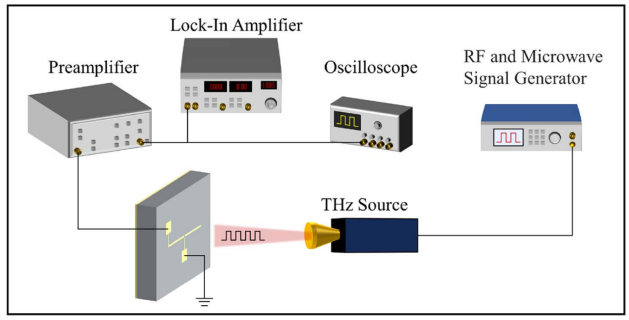

Fig. 9. Schematic diagram of the device measurement system.

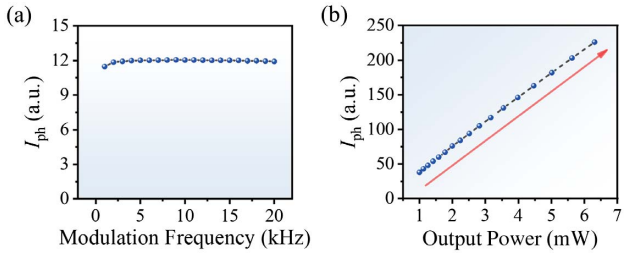

Fig. 10. (a) The response current at different modulation frequencies. (b) The response current at different output powers under 14.8 GHz illumination.

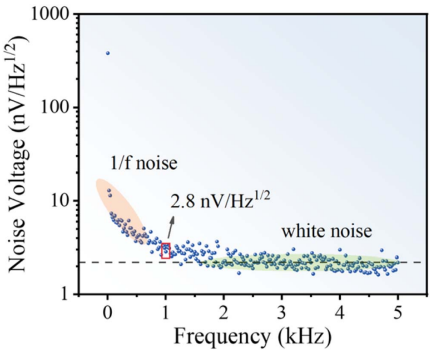

Fig. 11. The voltage noise density spectrum of the device measured at room temperature and in zero bias condition. The black dashed line is the Johnson–Nyquist white noise.

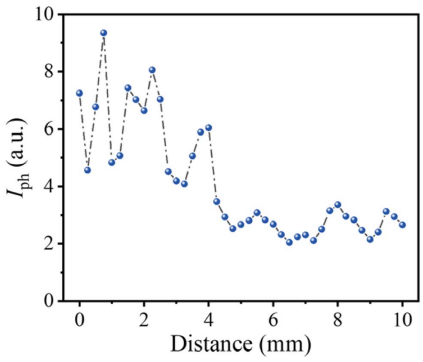

Fig. 12. Photocurrent with respect to the distance d at 99 GHz when the Au mirror is removed.

at the frequency of 1 kHz, which is consistent with the theoretical Johnson–Nyquist noise (2.3 nV/Hz$^{1/2}$).

APPENDIX D: DOUBLE-CAVITY MODEL

In order to obtain the true enhancement factor of the Fabry–Perot resonant cavity, we established a double-cavity model to exclude the enhancement induced by the reflection of the electric field from the emission port of the THz source. The surface of our device is set as the reference point of phase, and the electric field intensity E_n at the device surface can be calculated by the following expression:

$$E_n = \frac{2E_0(1 - r_e^n \cdot e^{2nh})}{1 - r_e \cdot e^{2h}}, \tag{D1}$$

where r_e is the equivalent reflectivity of the emission port, which is relevant to the distance between the detector and the THz source and decreases with the increase of the distance. The pseudo enhancement coefficient can be calculated by the following expression:

$$n = \frac{E_n}{2E_0}. \tag{D2}$$

It can be obtained by the numerical calculation that n is 3.74, that is, the pseudo enhancement factor induced by the reflection from the emission port is 3.74.

When the Au mirror is not mounted at the bottom of the silicon substrate, the double-cavity effect reduces greatly. The maximum peak-to-valley ratio Γ derived from Fig. 12 is 1.9, which is much smaller than the case of the Au mirror mounted ($\Gamma = 1177$).

APPENDIX E: PARAMETERS OF THE TWO-TEMPERATURE HEAT TRANSPORT MODEL

The parameter values taken in the calculation are listed in Table 2.

Funding. National Key Research and Development Program of China (2023YFF0719200); National Natural Science Foundation of China (61731020, 61988102); Science and Technology Commission of Shanghai Municipality (21S31907400).

Disclosures. The authors declare no conflicts of interest.

Table 2. Parameters of the Heat Transport Model

Parameter	Value	Parameter	Value
τ_{ep}	0.5 ns	τ	0.5 ns
T_0	300 K	κ_p	1000 W/(m · K) [48]
C_p	710 J/(kg · K) [49]	κ	318 W/(m · K)
C	128.0 J/(kg · K)	m	57
v_F	10^6 m/s [39]	Δ	0.1 eV [39]
E_F	0.1 eV	Thickness of Au film	40 nm
Q	3.0×10^6 W/m^2	ρ	1.93×10^4 kg/m^3
ρ_p	2.33×10^3 kg/m^3	μ_c	1000.0 cm^2/(V · m)

Data Availability. Data underlying the results presented in this paper are not publicly available at this time but may be obtained from the authors upon reasonable request.

REFERENCES

1. O. Ajakaiye, J. Grade, C. Shin, *et al.*, "Wafer-scale fabrication of infrared detectors based on tunneling displacement transducers," Sens. Actuators A **134**, 575–581 (2007).
2. H. C. Liu, C. Y. Song, A. J. SpringThorpe, *et al.*, "Terahertz quantum-well photodetector," Appl. Phys. Lett. **84**, 4068–4070 (2004).
3. A. El Fatimy, R. L. Myers-Ward, A. K. Boyd, *et al.*, "Epitaxial graphene quantum dots for high-performance terahertz bolometers," Nat. Nanotechnol. **11**, 335–338 (2016).
4. A. Dobroiu, M. Yamashita, Y. N. Ohshima, *et al.*, "Terahertz imaging system based on a backward-wave oscillator," Appl. Opt. **43**, 5637–5646 (2004).
5. R. Tauk, F. Teppe, S. Boubanga, *et al.*, "Plasma wave detection of terahertz radiation by silicon field effects transistors: responsivity and noise equivalent power," Appl. Phys. Lett. **89**, 253511 (2006).
6. M. S. Vitiello, D. Coquillat, L. Viti, *et al.*, "Room-temperature terahertz detectors based on semiconductor nanowire field-effect transistors," Nano Lett. **12**, 96–101 (2012).
7. L. Vicarelli, M. S. Vitiello, D. Coquillat, *et al.*, "Graphene field-effect transistors as room-temperature terahertz detectors," Nat. Mater. **11**, 865–871 (2012).
8. L. Viti, J. Hu, D. Coquillat, *et al.*, "Black phosphorus terahertz photodetectors," Adv. Mater. **27**, 5567–5572 (2015).
9. K. S. Novoselov, A. K. Geim, S. V. Morozov, *et al.*, "Two-dimensional gas of massless Dirac fermions in graphene," Nature **438**, 197–200 (2005).
10. Y. Zhang, Y.-W. Tan, H. L. Stormer, *et al.*, "Experimental observation of the quantum Hall effect and Berry's phase in graphene," Nature **438**, 201–204 (2005).
11. K. I. Bolotin, K. J. Sikes, Z. Jiang, *et al.*, "Ultrahigh electron mobility in suspended graphene," Solid State Commun. **146**, 351–355 (2008).
12. J.-H. Chen, C. Jang, S. Xiao, *et al.*, "Intrinsic and extrinsic performance limits of graphene devices on SiO_2," Nat. Nanotechnol. **3**, 206–209 (2008).
13. R. R. Nair, P. Blake, A. N. Grigorenko, *et al.*, "Fine structure constant defines visual transparency of graphene," Science **320**, 1308 (2008).
14. K. F. Mak, L. Ju, F. Wang, *et al.*, "Optical spectroscopy of graphene: from the far infrared to the ultraviolet," Solid State Commun. **152**, 1341–1349 (2012).
15. X. Cai, A. B. Sushkov, R. J. Suess, *et al.*, "Sensitive room-temperature terahertz detection via the photothermoelectric effect in graphene," Nat. Nanotechnol. **9**, 814–819 (2014).
16. M. Mittendorff, S. Winnerl, J. Kamann, *et al.*, "Ultrafast graphene-based broadband THz detector," Appl. Phys. Lett. **103**, 021113 (2013).
17. D. Spirito, D. Coquillat, S. L. De Bonis, *et al.*, "High performance bilayer-graphene terahertz detectors," Appl. Phys. Lett. **104**, 061111 (2014).
18. A. Zak, M. A. Andersson, M. Bauer, *et al.*, "Antenna-integrated 0.6 THz FET direct detectors based on CVD graphene," Nano Lett. **14**, 5834–5838 (2014).
19. A. A. Balandin, S. Ghosh, W. Bao, *et al.*, "Superior thermal conductivity of single-layer graphene," Nano Lett. **8**, 902–907 (2008).
20. Y. Xu, Z. Li, and W. Duan, "Thermal and thermoelectric properties of graphene," Small **10**, 2182–2199 (2014).
21. T. Y. Kim, C.-H. Park, and N. Marzari, "The electronic thermal conductivity of graphene," Nano Lett. **16**, 2439–2443 (2016).
22. M. Engel, M. Steiner, A. Lombardo, *et al.*, "Light–matter interaction in a microcavity-controlled graphene transistor," Nat. Commun. **3**, 906 (2012).
23. M. Furchi, A. Urich, A. Pospischil, *et al.*, "Microcavity-integrated graphene photodetector," Nano Lett. **12**, 2773–2777 (2012).
24. J. Wang, J. Hu, P. Becla, *et al.*, "Resonant-cavity-enhanced mid-infrared photodetector on a silicon platform," Opt. Express **18**, 12890–12896 (2010).
25. C. L. Canedy, W. W. Bewley, C. D. Merritt, *et al.*, "Resonant-cavity infrared detector with five-quantum-well absorber and 34% external quantum efficiency at 4 μm," Opt. Express **27**, 3771–3781 (2019).
26. N. Sefidmooye Azar, J. Bullock, V. R. Shrestha, *et al.*, "Long-wave infrared photodetectors based on 2D platinum diselenide atop optical cavity substrates," ACS Nano **15**, 6573–6581 (2021).
27. J. Zhou, J. Deng, M. Shi, *et al.*, "Cavity coupled plasmonic resonator enhanced infrared detectors," Appl. Phys. Lett. **119**, 160504 (2021).
28. G. C. Dyer, S. Preu, G. R. Aizin, *et al.*, "Enhanced performance of resonant sub-terahertz detection in a plasmonic cavity," Appl. Phys. Lett. **100**, 083506 (2012).
29. W. Cheng, Z. Han, Y. Du, *et al.*, "Highly sensitive terahertz fingerprint sensing with high-*Q* guided resonance in photonic crystal cavity," Opt. Express **27**, 16071–16079 (2019).
30. B. Rethfeld, D. S. Ivanov, M. E. Garcia, *et al.*, "Modelling ultrafast laser ablation," J. Phys. Appl. Phys. **50**, 193001 (2017).
31. A. Alù and N. Engheta, "Tuning the scattering response of optical nanoantennas with nanocircuit loads," Nat. Photonics **2**, 307–310 (2008).
32. X. He, X. Wang, S. Nanot, *et al.*, "Photothermoelectric p–n junction photodetector with intrinsic broadband polarimetry based on macroscopic carbon nanotube films," ACS Nano **7**, 7271–7277 (2013).
33. F. Wang, T. Zhang, R. Xie, *et al.*, "How to characterize figures of merit of two-dimensional photodetectors," Nat. Commun. **14**, 2224 (2023).
34. J. Duan, X. Wang, X. Lai, *et al.*, "High thermoelectric power factor in graphene/hBN devices," Proc. Natl. Acad. Sci. USA **113**, 14272–14276 (2016).
35. A. P. Aji, C. Apriono, and E. T. Rahardjo, "Input power and effective area in terahertz detector measurement: a review," IEEE Access **11**, 29323–29343 (2023).
36. W. L. Stutzman and G. A. Thiele, *Antenna Theory and Design*, 3rd ed. (Wiley, 2012).
37. J. Pettine, P. Padmanabhan, T. Shi, *et al.*, "Light-driven nanoscale vectorial currents," Nature **626**, 984–989 (2024).
38. R. Negishi, C. Wei, Y. Yao, *et al.*, "Turbostratic stacking effect in multilayer graphene on the electrical transport properties," Phys. Status Solidi B **257**, 1900437 (2020).
39. M. Massicotte, G. Soavi, A. Principi, *et al.*, "Hot carriers in graphene—fundamentals and applications," Nanoscale **13**, 8376–8411 (2021).
40. W. Guo, L. Wang, X. Chen, *et al.*, "Graphene-based broadband terahertz detector integrated with a square-spiral antenna," Opt. Lett. **43**, 1647–1650 (2018).
41. L. Viti, D. G. Purdie, A. Lombardo, *et al.*, "HBN-encapsulated, graphene-based, room-temperature terahertz receivers, with high speed and low noise," Nano Lett. **20**, 3169–3177 (2020).
42. M. Asgari, E. Riccardi, O. Balci, *et al.*, "Chip-scalable, room-temperature, zero-bias, graphene-based terahertz detectors with nanosecond response time," ACS Nano **15**, 17966–17976 (2021).
43. M. Chen, Y. Wang, J. Wen, *et al.*, "Annealing temperature-dependent terahertz thermal–electrical conversion characteristics of three-dimensional microporous graphene," ACS Appl. Mater. Interfaces **11**, 6411–6420 (2019).
44. M. Chen, Y. Wang, W. Ma, *et al.*, "Ionic liquid gating enhanced photothermoelectric conversion in three-dimensional microporous graphene," ACS Appl. Mater. Interfaces **12**, 28510–28519 (2020).
45. D. A. Bandurin, I. Gayduchenko, Y. Cao, *et al.*, "Dual origin of room temperature sub-terahertz photoresponse in graphene field effect transistors," Appl. Phys. Lett. **112**, 141101 (2018).
46. M. Dai, C. Wang, B. Qiang, *et al.*, "Long-wave infrared photothermoelectric detectors with ultrahigh polarization sensitivity," Nat. Commun. **14**, 3421 (2023).
47. X. Wang, "Uncooled CMOS integrated triple-band terahertz thermal detector comprising of metamaterial absorber and PTAT sensor," IEEE Access **8**, 114501 (2020).
48. K. Chu, X. Wang, Y. Li, *et al.*, "Thermal properties of graphene/metal composites with aligned graphene," Mater. Des. **140**, 85–94 (2018).
49. N. K. Mahanta and A. R. Abramson, "Thermal conductivity of graphene and graphene oxide nanoplatelets," in *13th InterSociety Conference on Thermal and Thermomechanical Phenomena in Electronic Systems* (2012), pp. 1–6.